ELSEVIER

Polymer 42 (2001) 9955–9967

polymer

www.elsevier.com/locate/polymer

Experimental characterization of electrospinning: the electrically forced jet and instabilities

Y.M. Shin[a], M.M. Hohman[b], M.P. Brenner[c], G.C. Rutledge[d,*]

[a]Department of Materials Science and Engineering, Massachusetts Institute of Technology, 77 Massachusetts Avenue, Cambridge, MA 01239, USA
[b]Department of Physics, James Franck Institute, University of Chicago, 5640 Ellis Avenue, Chicago, IL 60637, USA
[c]Department of Mathematics, Massachusetts Institute of Technology, 77 Massachusetts Avenue, Cambridge, MA 01239, USA
[d]Department of Chemical Engineering, Massachusetts Institute of Technology, 77 Massachusetts Avenue, Cambridge, MA 01239, USA

Received 9 May 2001; received in revised form 23 July 2001; accepted 25 July 2001

Abstract

In the electrospinning process, polymer fibers with submicron-scale diameters are formed by subjecting a fluid jet to a high electric field. We report an experimental investigation of the electrically forced jet and its instabilities. The results are interpreted within the framework of a recently developed theory for electrified fluid jets. We find that the process can be described by a small set of operating parameters and summarized through the use of operating diagrams of electric field versus flow rate. In addition, the jet current is related to the net charge density and found to depend on the fluid properties, the applied electric field and the equipment configuration. The net charge density appears to be relatively insensitive to the flow rate, at least for high flow rates. The experiments reveal that a key process in the formation of submicron-scale solid fibers is a convective instability, the rapidly whipping jet. The dependence of this instability on electric field and flow rate, and the exponential nature of its growth rate are in accord with the theory. © 2001 Elsevier Science Ltd. All rights reserved.

Keywords: Electrospinning; Electrified fluid jet; Instability

1. Introduction

Synthetic fibers of polymers have been produced for decades by conventional processes, such as melt spinning, dry spinning or wet spinning. These techniques rely upon pressure-driven extrusion of a viscous polymer fluid and produce fibers that typically range from 10 to 500 μm in diameter [1]. Electrostatic fiber spinning, or 'electrospinning,' is a novel process for forming fibers with submicron-scale diameters through the action of electrostatic forces. The small fiber diameters and the porous structure of electrospun fabrics result in a high specific surface area that is beneficial in a wide variety of applications. Proposed uses of electrospun fibers include filters, membranes, wound dressings, vascular grafts and tissue engineering scaffolds [2–4]. In addition, electrospun fibers may contain a static electric charge that further enhances filtration efficiency.

The first reference to the electrospinning process dates back to 1934 [5]. Since then, there have been exploratory studies of electrospinning of polymer melts [6–8]. Recently, it has been shown that the electrospinning process is capable of producing fibers with submicron-scale diameters [9], and these diameters are at least one order of magnitude smaller than those obtained by conventional fiber spinning. To date, over 30 synthetic or natural polymers have been electrospun, with research interest focusing primarily on the structure and morphology of electrospun fibers, e.g. [9–12]. In addition, there have been studies on the transport and permeability properties of electrospun non-woven textiles [13].

The basic elements of electrospinning are simple to implement. An electrode connected to a high voltage power supply is inserted into a polymeric solution contained within a capillary tube. A grounded collection plate or screen is placed at a distance of about 20 cm from the tip of the capillary tube. Initially, the polymer solution is held by its surface tension in the form of a droplet at the end of the capillary tube. As the voltage is increased, charge is induced on the fluid surface, and the droplet is distorted. Above a critical voltage, a single jet is ejected from the apex of a conical meniscus, commonly referred to as the Taylor cone [14]. Beyond the conical base immediately at the end of the capillary tube, the jet continues to thin. This jetting mode is known as the electrohydrodynamic cone-jet [15]. Prior to deposition on the collector, the jet may

* Corresponding author. Tel.: +1-617-253-0171; fax: +1-617-258-0546.
E-mail address: rutledge@mit.edu (G.C. Rutledge).

PII: S0032-3861(01)00540-7

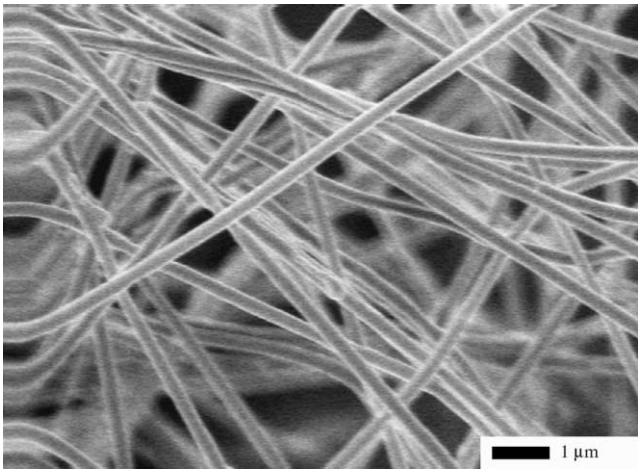

Fig. 1. SEM micrograph of fibers electrospun from a 2 wt% aqueous solution of PEO with an applied electric field of 0.3 kV cm^{-1} and a flow rate of 1 ml min^{-1}.

undergo a fluid instability that leads to accelerated solidification of the fluid jet and the collection of solid, charged fibers on the collector, usually in the form of a non-woven fabric. This instability was originally thought to be a single jet splitting into multiple filaments due to radial charge repulsion and was termed 'splaying' [9]. An SEM micrograph of electrospun poly(ethylene oxide) (PEO) fibers is shown in Fig. 1.

In spite of the surge in interest in the fibers and textiles produced by electrospinning, there has been relatively little attention to the process itself. A few investigations have reported the effects on the jet and fiber of selected fluid variables such as viscosity and polymer concentration, or operating parameters such as fluid flow rate, applied voltage, or the nature of the surrounding gas, with varying results [16–19]. However, the number of fluid, equipment and operating variables with potential to alter the behavior of the process are numerous and highly coupled. We are aware of no theory to date capable of describing this process with quantitative accuracy, which has hindered the consistent interpretation of experiments. On the other hand, the development of a relatively simple model of the process has been impeded by the lack of systematic, fully characterized experimental observations suitable to guide and test the theoretical development. Given these circumstances, we felt that a combined theoretical and experimental program was warranted. To this end, we have conducted a systematic experimental and theoretical investigation of the electrospinning process. A preliminary report describing our understanding of the fluid instability operative in electrospinning has already been presented [20]. Our theory for the fundamental electrohydrodynamics of electrified fluid jets is described in more detail elsewhere [21,22]. Here we present in detail the experimental observations and our interpretations within this new theoretical framework. We show that the jet formation and subsequent instability can be characterized by using a relatively small set of operating parameters. The organization of this paper is as follows: in Section 2, the experimental details are described. The results of the experimental study are presented in Section 3. The essential features of the theory are described in Section 4 and related to the experimental results. Section 5 summarizes the key findings of this study and discusses the implications for the underlying mechanism of electrospinning.

2. Experimental section

The apparatus used in this work was designed to ensure operation in a uniform electric field that is generated between two aluminum disks (100 mm diameter). The two disks are placed parallel to each other, thereby forming the geometry of a capacitor with parallel field lines. This 'parallel-plate' geometry distinguishes the current study from previous investigations, where the electric field was applied between a capillary tip or needle at high electric potential and a large grounded collector. For clarity, we refer to the latter configuration as a 'point-plate' geometry. Although the point-plate configuration is easier to implement, the resulting non-uniform electric field poses some complications for any subsequent theoretical analysis, as described later.

The stationary top plate is connected to a high voltage power supply (Gamma High Voltage Research, ES-30P). The fluid is fed at a constant volumetric flow rate to a stainless steel capillary tube, or nozzle (1.6 mm OD, 1 mm ID), in the center of the top plate. The flow rate is adjusted with a digitally controlled syringe pump (Harvard Apparatus, PHD 2000). The bottom plate acts as a collector and is aligned vertically with the top plate. Its height is adjusted manually to realize different spinneret-to-collector distances. The bottom plate is furthermore insulated from ground, and the jet current is measured as the voltage drop across a 10 kΩ resistor placed in series between the bottom plate and ground. The measurements were taken with a digital multimeter (Fluke, 85 III), and the readings were converted using Ohm's law. A schematic representation of the experimental system is shown in Fig. 2.

The variables affecting the behavior of the electrified fluid jet during electrospinning can be divided into fluid properties and operating parameters. The relevant fluid properties are viscosity (η), conductivity (K), dielectric constant (ϵ) and surface tension (γ). The operating parameters are flow rate (Q), jet current (I), applied electric potential (V) and distance (d) between the spinneret and the collector. The applied electric field (E_∞) is V/d.

Glycerol (Aldrich) and a 2 wt% aqueous solution of PEO (Aldrich, 2,000,000 g/mol) were chosen as model fluids. The fluid conductivity and viscosity were measured with a conductivity meter (Cole–Parmer, 19820) and a Couette viscometer (Bohlin, V88), respectively. Surface tension measurements were taken with a digital tensiometer

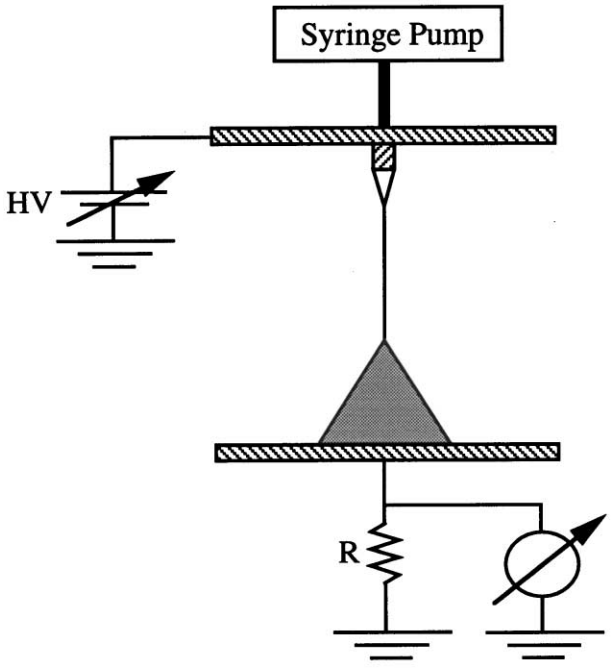

Fig. 2. Schematic representation of the parallel-plate fiber spinner. A uniform electric field is generated by applying a high voltage between two parallel plates. The polymer fluid is delivered to a metal capillary in the center of the top plate at a constant flow rate. The jet thins away from the nozzle and subsequently becomes unstable. The instability region is indicated by the grey region. Jet currents are determined by measuring the voltage drop across a resistor.

(Krüss, K10ST) using the Wilhelmy method. Literature values for the dielectric constants of glycerol and water (42.5 and 78.5, respectively [23]) were used; the dielectric constant of the aqueous PEO solution was assumed to be similar to that of water. The fluid properties are summarized in Table 1.

Stable jets were studied with a long distance microscope (Infinity Photo-Optical Co., K2) connected to a manual focus 35 mm SLR camera (Canon), resulting in magnifications of up to 20×. The camera was mounted on a tripod and translated vertically to image different segments of the jet. To improve image contrast, the jet was backlit with an area backlight (Dolan Jenner, QVABL-48 and Fiber-Lite PL-750). The images were taken on conventional film, digitized at 1000 dpi and edge-detected using IDL® software (Research Systems, Boulder, CO).

Table 1
Properties of model fluids

	Glycerol	PEO–water solution
Viscosity (cP)	1490	1670
Conductivity (μS/cm)	0.01	120
Dielectric constant	42.5[a]	78.5[a,b]
Surface tension (mN/m)	64	60.5

[a] From Ref. [23].
[b] Dielectric constant for water.

The instability in electrospinning occurs very rapidly, which requires the use of high-speed photographic techniques. For real-time evaluation of the process dynamics, the jet was illuminated with a strobe (GenRad, 1538-A). In addition, details of the motion were visualized by illumination with a fast (18 ns, nominal) flash (High Speed Photo Systems, Nanolite driver and KL-L lamp). The flash was synchronized with the shutter of the camera, and bellows were used to obtain a magnification of 5×.

'Operating diagrams' delineate regions of different jet behaviors as a function of the applied electric field and flow rate. Similar diagrams were proposed by Cloupeau and Prunet-Foch for electrosprays [15]. Procedurally, we measured these diagrams by choosing a particular flow rate and then cycling the applied voltage between zero and our maximum voltage of 30 kV. As the voltage is increased from 0 kV, the fluid first begins to drip out of the nozzle. The dripping frequency increases as the voltage is increased, until a transition is observed from dripping to a stable jet at a voltage denoted by V_{stable}. A jet was deemed stable when no surface perturbations in the conical base region were visible. The voltage is then further increased to the maximum voltage, and if an additional transition from a stable jet to a second, unstable jet is observed at high field, this is denoted by V_{whip}. Upon lowering the voltage, the stable jet again begins to drip at a voltage denoted by V_{drip}, which may differ from V_{stable}. Generally, no such hysteresis was detectable for V_{whip}. Measurements were reproducible to within ±0.2 kV. This cycling of applied voltage was repeated at successively higher flow rates in order to map out bounds for each transition. At sufficiently high flow rates, a stable jet is observed even at zero applied field. All of the aforementioned critical voltages were normalized by the plate separation distance and expressed as electric fields, E_{stable}, E_{drip} and E_{whip}. The plate separations were chosen so that the transitions could be observed at the voltages attainable with the power supply. Since no instabilities could be observed in glycerol before dielectric breakdown occurred, the plate distance was set to 6 cm. For the PEO–water solution, the plate distance was set to 15 cm.

3. Results and discussion

3.1. Glycerol

Stable jets. For a given fluid, the electric field and flow rate affect the shape of the jet. As the electric field is increased, the jet thins more rapidly, and the cone region becomes shorter and more concave in profile [22]. This change in cone shape is in accord with prior results by Hayati [24], who determined the velocity profile in the conical region of an electrified fluid jet using streak photography of tracer particles. The photographs revealed an axisymmetric circulation pattern, with the maximum flow rate directed toward the apex on the surface of the Taylor

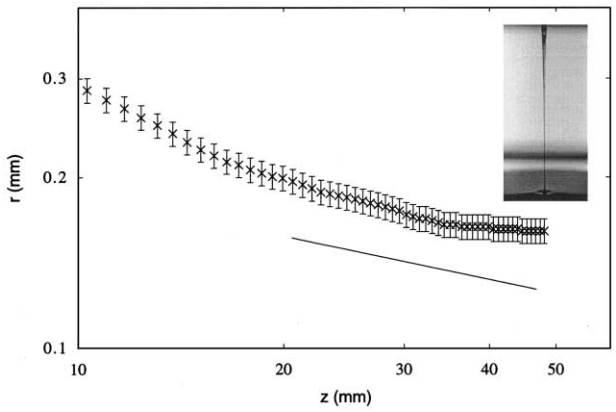

Fig. 3. Radius r of jet versus axial distance z from nozzle for a stable jet of glycerol ($E_\infty = 2$ kV cm^{-1}, $Q = 6$ ml min^{-1}). The nozzle protrusion is 7.2 mm. The solid line corresponds to the slope of a line that scales as $r \propto z^{-0.25}$. The error bars indicate the width of the jet profile edges.

cone and backflow away from the apex at the centerline of the cone. The origin of this axisymmetric motion was attributed to the presence of tangential electrical shear stresses [25] at the surface of the cone. At high electric fields, more fluid is sheared off the surface of the cone, resulting in pronounced concave cone shapes.

Beyond the Taylor cone, the jet thins slowly. Images of the steady jet were taken for electric fields between 2 and 5 kV cm^{-1}, and flow rate ranging from 0.5 to 7 ml min^{-1}. From these images, the radius of the jet as a function of axial distance from the nozzle was determined for several sets of operating conditions. Fig. 3 shows the scaling of the jet radius as a function of the axial distance for a glycerol jet at an applied electric field of 2 kV cm^{-1} and a flow rate of 6 ml min^{-1}. Sufficiently far from the Taylor cone region, the experimental profile is in reasonable accord with the theoretical asymptotic scaling of $r \propto z^{-0.25}$ (c.f. Section 4) [26].

Jet currents. Jet currents were measured as a function of the applied electric field and flow rate. To avoid spurious results due to displacement currents and corona discharge, current measurements were taken in DC mode, and the plate separation in each experiment was made sufficiently large such that at an applied voltage of 30 kV (the maximum possible with our equipment), no current was detected in the absence of a jet. The jet currents were subsequently converted to net charge densities ρ_e (C/cm^3) $= I/Q$. This charge includes both surface and bulk charges; however, sufficiently far from the nozzle, the net charge should be comprised entirely of surface charge.

Due to its low conductivity, glycerol requires high electric fields to obtain stable jets. Experimentally, this requires either high voltages and/or low plate separations, both of which were found to be problematic for measuring jet currents accurately. However, starting from a nozzle that was effectively 'flush' with the top plate (i.e. the nozzle protrudes less than 0.2 mm from the surface of the plate), we also observed that stable glycerol jets could be obtained at lower voltages merely by increasing the nozzle protrusion from the top plate. This observation is in accord with the analysis of Taylor, who determined the critical voltage at which a jet or droplet appears [27]. As the nozzle protrusion increases, the electric force acting on the fluid increases and therefore, a lower voltage is required to initiate the jet.

The increased force can be rationalized by considering the change in shape of the electric field (a 'fringe field') due to the protrusion of the nozzle from the top plate, both of which are at the same potential (c.f. Section 4). In the immediate vicinity of the nozzle, the electric field is higher, but it decays over a short distance to the nominal applied electric field between the plates. For a nozzle protrusion of 7.2 mm, Fig. 4(a) shows the relation between current and electric field for glycerol. The measured jet currents are in the nanoampere range, which correspond to net charge densities in the range 2–16 μC cm^{-3}. The relationship between current and flow rate is shown in Fig. 4(b). These observations suggest that current scales linearly with both electric field and flow rate. The total charge density is shown in Fig. 4(c).

Glycerol operating diagram. Fig. 5 shows an operating diagram for glycerol. At low flow rates and electric fields, dripping is observed. At higher flow rates or electric fields, a stable jet is obtained. The data for E_{stable} and E_{drip} indicate a transition from a regime of operation apparently unstable to the Rayleigh breakup mode to a regime of stable jet operation, and vice versa. A mild hysteresis between the onset and disruption of a stable jet is observed. The theoretical operating diagram (c.f. Section 4) is shown as the shaded region in Fig. 5. Unstable jets of the second type, associated with high electric fields, were not observed with glycerol for the electric fields attainable with our equipment; consideration of this observation in the context of the theoretical model suggests that this is largely a consequence of the low conductivity of glycerol.

3.2. PEO–water solution

Stable jets. Fig. 6 shows profiles of stable PEO–water jets. The flow rate is 0.1 ml min^{-1} and the electric fields range from 0.47 to 1.0 kV cm^{-1} (from left to right). At an applied electric field of 1 kV cm^{-1}, the Taylor cone is no longer observed; the jet seems to emanate directly from the nozzle. This has also been observed by Deitzel et al. [19]. We conjecture that either the Taylor cone has moved inside the nozzle or the tangential electrical stress shears off fluid rapidly so that there is not sufficient fluid for the formation of the Taylor cone. The difference in Taylor cone shapes between glycerol (c.f. Fig. 9 of Ref. [22]) and the PEO–water solution can be attributed to the large difference in conductivity between the two model fluids.

Jet currents. Fig. 7(a) shows the relationship between current and electric field for the PEO–water solution. The jet currents are in the microampere range, which is attributed to the high conductivity of the PEO–water solution. As seen before with glycerol, the relation between

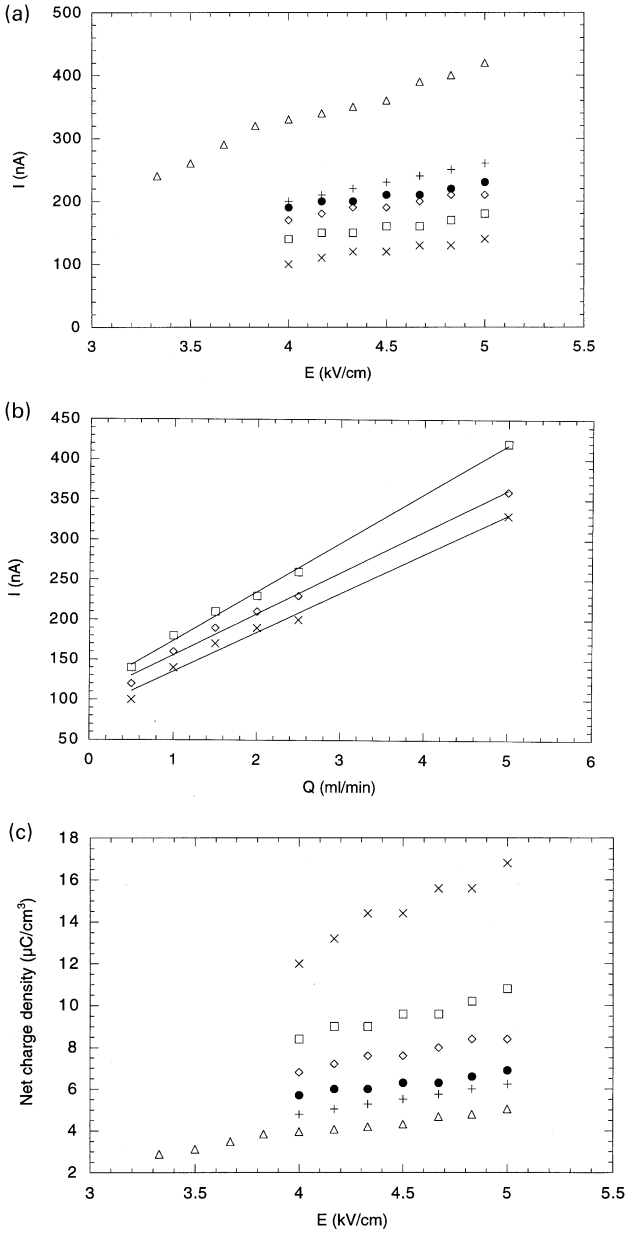

Fig. 4. Electric currents in stable glycerol jets. The nozzle protrusion is 7.2 mm. (a) Relation between current and electric field. (×) $Q = 0.5$ ml min^{-1}, (□) $Q = 1$ ml min^{-1}, (◇) $Q = 1.5$ ml min^{-1}, (●) $Q = 2$ ml min^{-1}, (+) $Q = 2.5$ ml min^{-1} and (△) $Q = 5$ ml min^{-1}. (b) Relation between current and flow rate. (×) $E_\infty = 4$ kV cm^{-1}, (◇) $E_\infty = 4.5$ kV cm^{-1} and (□) $E_\infty = 5$ kV cm^{-1}. The solid lines were obtained by linear regression. (c) Net charge density. The symbols correspond to the same flow rates as in (a).

current and electric field is linear for low flow rates. However, at higher flow rates, a transition between 1 and 1.5 kV cm^{-1} is observed. This transition coincides with the onset of instabilities. Below 1 kV cm^{-1}, the jet is stable and follows a straight path. Between 1 and 1.5 kV cm^{-1}, the jet starts bending, which eventually turns into a whipping motion. This is described further below. Fig. 7(b) shows the relation between current and flow rate. Again, the

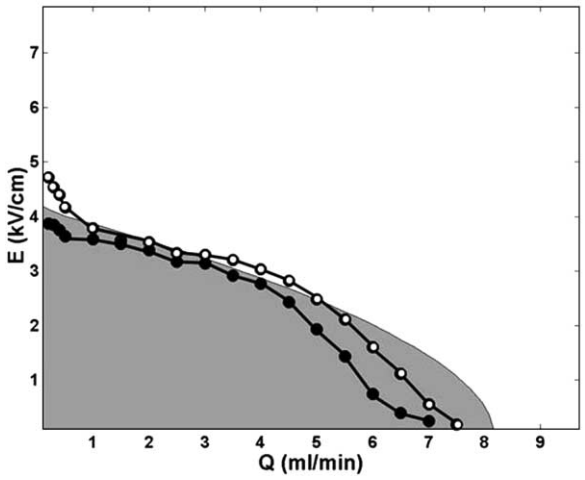

Fig. 5. Operating diagram for glycerol. Symbols indicate experimental data. Filled circles: E_{drip}; open circles: E_{stable}. The shaded regions are determined by the theory (see text for details). Theoretical transitions are based on the contours of $\Gamma(E_\infty, Q) = 2\pi$. Light region: stable jet; grey region: Rayleigh unstable.

current scales linearly with both applied electric field and flow rate in each of the two regimes. The observed jet currents correspond to net charge densities in the range 200–2000 μC cm^{-3}, which is shown in Fig. 7(c). Previous investigators [18,28] report a quadratic dependence of current on field strength; in those experiments, however, the flow rate appears not to be held constant, but allowed to increase (linearly, in fact [28]) in response to higher electric fields. The reported currents are an order of magnitude lower; this could be due to differences in solution properties (e.g. conductivity) or equipment configuration.

In Fig. 7(a), higher currents are associated with higher flow rates. In Fig. 7(c), the current has been normalized by the flow rate, and the data for different flow rates collapse onto a single curve. The agreement is especially good for flow rates between 0.5 and 1.5 ml min^{-1} and outside the transition region (1–1.5 kV cm^{-1}). Due to the small currents, the observed differences in net charge density are in the range of experimental error. This seems to imply that while the net charge density is correlated with the applied electric field, it is independent of the flow rate. A detailed investigation of the charge transfer mechanism from the nozzle to the fluid may provide further insight, but is beyond the scope of this report.

With its higher conductivity, the PEO–water solution exhibits stable jet behavior at lower field strengths compared to glycerol. With this fluid, we were able to assess the difference between parallel-plate and point-plate configurations by changing the distance by which the nozzle protrudes from the top plate. Fig. 8 shows the jet current measured for two nozzle protrusion distances, 0.20 and 3.67 mm, for flow rates of 0.1, 0.5 and 1.5 ml min^{-1}, and applied fields ranging from 0.5 to 2.0 kV cm^{-1}. The configuration with larger protrusion initiates stable jet operation at lower applied electric fields in accord with Taylor's analysis

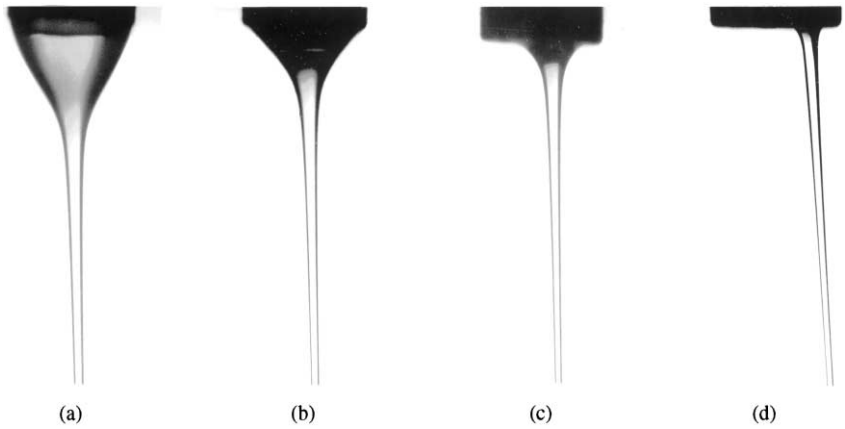

Fig. 6. Stable jet profiles of PEO–water. The nozzle protrusion is 3.76 mm. $Q = 0.1$ ml min^{-1} and (a) $E_\infty = 0.47$, (b) $E_\infty = 0.53$, (c) $E_\infty = 0.6$ and (d) $E_\infty = 1$ kV cm^{-1}.

[27]. However, the current measured is lower for the same applied field strength. The effect of the nozzle protrusion on the jet current is related to the charge transfer mechanism at the nozzle and presently not understood.

Operating diagram. An operating diagram for the PEO–water solution is shown in Fig. 9. The suppression of the Rayleigh instability and the hysteresis between the onset and disruption of a stable jet are similar to that observed in glycerol. Upon increasing the electric field further, a second transition from a stable jet to an unstable jet, characterized by bending oscillations of the jet centerline, is observed. The stability border between stable and unstable jets is not linear but displays a pronounced curvature. The theoretical predictions are indicated by the shaded regions. Operation of the process in the region above the second transition results in the production of solid, submicron diameter fibers that are of interest for fiber and textile applications. Operation in the stable jet region results only in deposition and coalescence of fluid on the collector. We suggest that the transformation of fluid to solid fiber is a direct consequence of this second instability that is responsible for the accelerated solidification of the fluid jet into solid fibers. The precise manner in which this instability could promote solidification depends crucially on the nature of the instability and is discussed further below.

The whipping instability. The high field instability is perceived to be crucial in the formation of submicron-scale fibers by electrospinning. When viewed with exposure times down to the millisecond range, the instability zone has the appearance of a conical region, which opens outward in the direction of flow, suggestive of an envelope of multiple jets. This is shown in Fig. 10(a). Using high-speed photography, we observe that this conical envelope in Fig. 10(a) is attributable to a single, rapidly 'whipping' jet. The frequency of the whipping motion is so fast that conventional photography lends the appearance of splitting into multiple filaments. Fig. 10(b) shows a double-exposure image of the instability. The instability was illuminated from behind with an 18 ns flash and the whipping jet is seen as a dark line. In addition, front illumination with a continuous light source shows the envelope. The whipping motion is in accord with previous observations [16,29,30]. Beyond the onset of the instability, the whipping motion becomes more chaotic and extensive bending can be observed. Due to the large illuminated area, the energy of the flash (25 mJ) results in relatively low contrast. To improve the visibility, a trace of the jet path is shown in Fig. 10(c). It is significant that the amplitude of the instability grows as it is convected downstream, which is useful for the formulation of the theory as described in Section 4.

In order to estimate the growth of the whipping instability mode, we analyzed images of the conical envelope of the instability zone obtained from long exposure photographs. The envelope was traced, plotted as a function of the distance from the cone apex and fitted with an exponential function to obtain an estimate of the growth rate. An example is shown in Fig. 11, where the data for an electric field of 1.11 kV cm^{-1} and a flow rate of 0.2 ml min^{-1} is shown. The data are reasonably well described by an equation of the form $\ln[A(z)/A_0] = (\omega z)/U_0$ where U_0 is the average fluid velocity at the nozzle and $\omega = 0.014 \pm 0.002$ s^{-1}. Determination of a growth constant in this manner is subject to about 10% uncertainty as a result of variation in the lighting conditions and image quality. As the applied electric field is increased, the growth rate increases. At an electric field of 1.47 kV cm^{-1} and a flow rate of 0.2 ml min^{-1}, $\omega = 0.020 \pm 0.002$ s^{-1}. This trend is in qualitative accord with the theoretical prediction that the growth rate scales with the applied electric field.

4. Comparison to theory

4.1. The electrohydrodynamic equations

The theoretical approach presented here is based on our

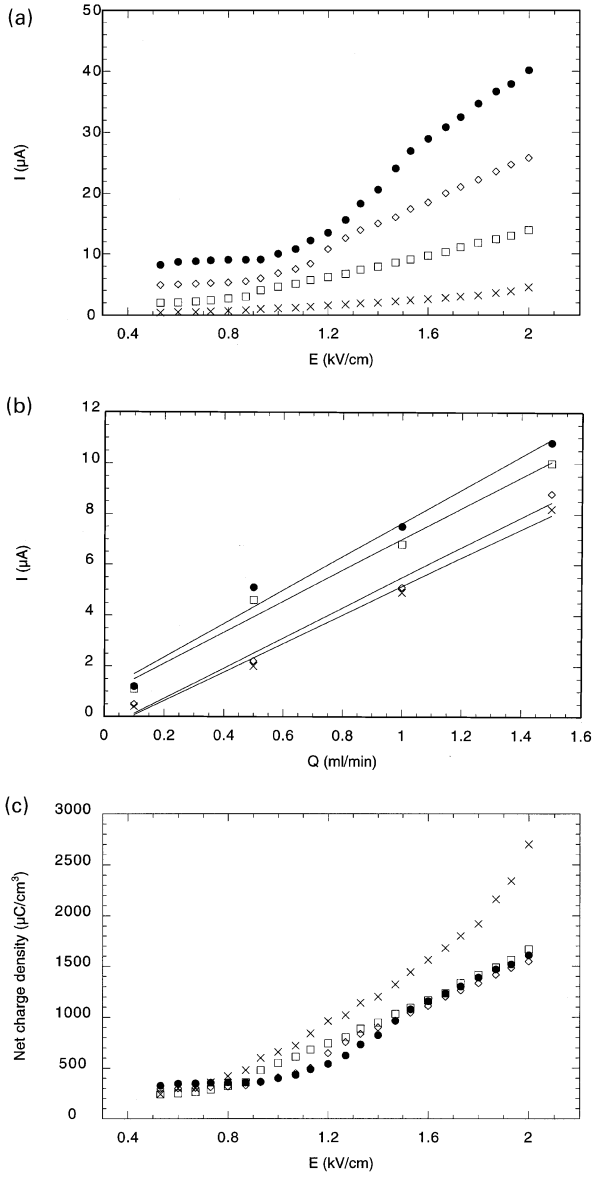

Fig. 7. Electric currents in stable PEO–water jets. The nozzle protrusion is 3.76 mm. (a) Relation between current and electric field. (×) $Q = 0.1$ ml min^{-1}, (□) $Q = 0.5$ ml min^{-1}, (◇) $Q = 1$ ml min^{-1} and (●) $Q = 1.5$ ml min^{-1}. (b) Relation between current and flow rate. (×) $E_\infty = 0.53$ kV cm^{-1}, (◇) $E_\infty = 0.67$ kV cm^{-1}, (□) $E_\infty = 1.93$ kV cm^{-1} and (●) $E_\infty = 2$ kV cm^{-1}. The solid lines were obtained from linear regression. (c) Net charge density. The symbols correspond to the same flow rates as in (a).

empirical observation that the instabilities occur on a length scale much longer than the jet radius. This motivates us to represent the jet as a long, slender object. As a first step, we have assumed that the fluid is Newtonian and incompressible. Treatment of more complex, e.g. viscoelastic, fluid behavior should also be possible without major revision of the basic theoretical approach. A more detailed exposition of the mathematical development is presented elsewhere [21,22], and only the key aspects are summarized here.

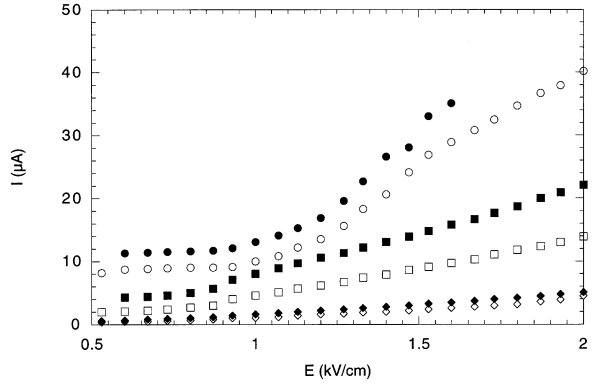

Fig. 8. Effect of the nozzle protrusion on jet current measurements. Solid symbols: nozzle protrusion = 0.2 mm; open symbols: nozzle protrusion = 3.76 mm. (◇) $Q = 0.1$ ml min^{-1}, (□) $Q = 0.5$ ml min^{-1} and (○) $Q = 1.5$ ml min^{-1}.

The relevant three-dimensional variables — radial velocity (v_r), axial velocity (v_z), radial electric field (E_r) and axial electric field (E_z) — are expanded as Taylor series in the jet radius. These expansions are substituted into the full three-dimensional equations for conservation of mass, conservation of charge and differential momentum balance, and only the leading order terms are retained. Due to viscous dissipation and external forcing by both gravity and the electric field, the isolated system of the jet does not conserve energy.

The resulting hydrodynamic equations are made non-dimensional by choosing a length scale r_0, where r_0 is the diameter of the capillary; a time scale $t_0 = \sqrt{\rho r_0^3/\gamma}$, where γ is the surface tension and ρ is the density of the fluid; an

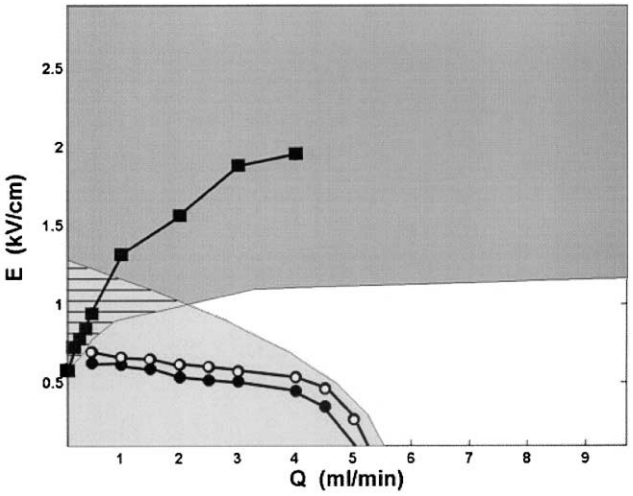

Fig. 9. Operating diagram for PEO–water. Symbols indicate experimental data. Filled circles: E_{drip}; open circles: E_{stable}, filled squares: E_{whip}. The shaded regions are determined by the theory (see text for details). Theoretical transitions are based on the contours of $\Gamma(E_\infty, Q) = 2\pi$. Light region: stable jet; light grey region: Rayleigh unstable; dark grey region: whipping unstable. In the crosshatched region, the theoretical Rayleigh and whipping instabilities are of comparable magnitude.

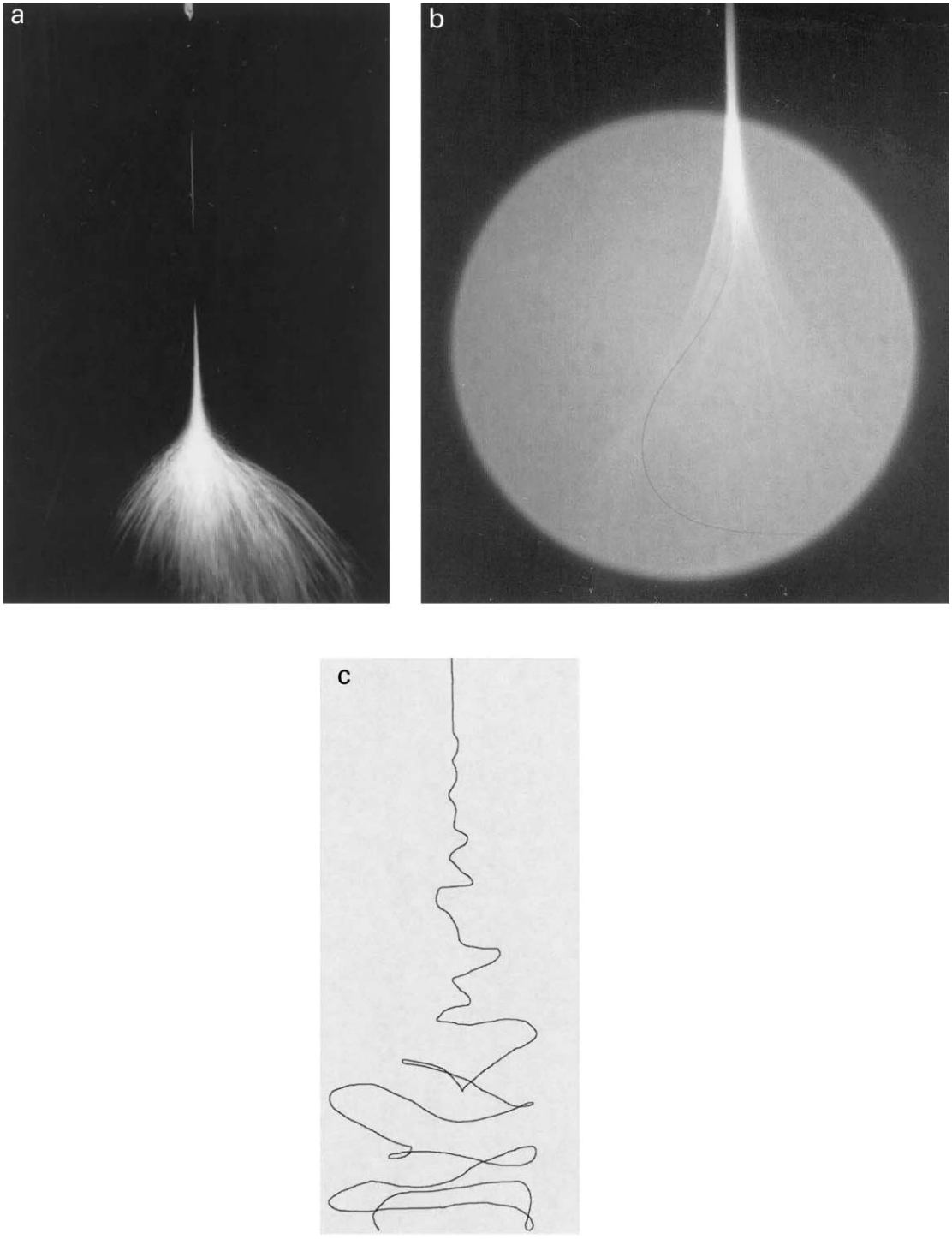

Fig. 10. (a) Instability region in an electrified PEO–water jet. The exposure time is 1/250 s. Vertical distance = 9 cm. (b) Instability region in an electrified PEO–water jet. Superposition of the whipping jet (exposure time = 18 ns) and the envelope (exposure time = 1/250 s). The whipping jet can be seen as a dark line. Diameter of circle = 15 mm. (c) Instability region in an electrified PEO–water jet. The exposure time is 18 ns and a trace of the jet in the entire instability region is shown. Vertical distance = 20 cm.

electric field strength $E_0 = \sqrt{\gamma/(\epsilon - \bar{\epsilon})r_0}$ where $\epsilon(\bar{\epsilon})$ is the permittivity of the fluid (air); and a surface charge density $\sqrt{\gamma\bar{\epsilon}/r_0}$. The dimensionless asymptotic field is $\Omega_0 = E_\infty/E_0$. The material properties of the fluid are characterized by four dimensionless parameters; $\beta = \epsilon/\bar{\epsilon} - 1$; the dimensionless viscosity $\nu^* = \sqrt{\nu^2/(\rho\gamma r_0)}$; the dimensionless gravity $g^* = g\rho r_0^2/\gamma$; and the dimensionless conductivity $K^* = K\sqrt{\rho r_0^3/(\beta\gamma)}$. The non-dimensionalized equations for conservation of mass and conservation of charge, and the Navier–Stokes equation are shown in Eqs. (1)–(3),

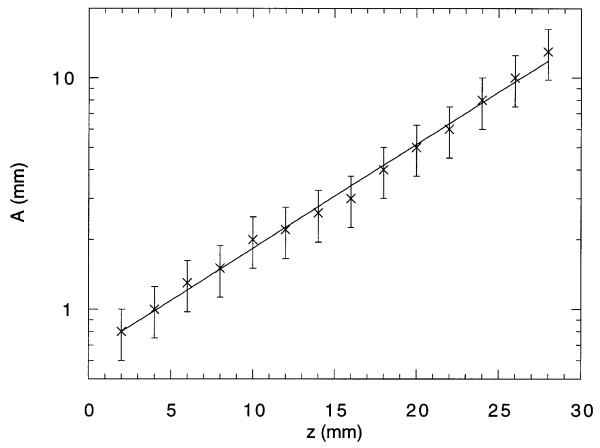

Fig. 11. Amplitude A of whipping instability, as estimated from the radius of the instability envelope, versus axial distance z from the onset of the instability. The envelope of the instability can be fitted with an equation of the form $\ln[A(z)/A_0] = (\omega z)/U_0$ where $\omega = 0.014 \pm 0.002$. Error bars are indicative of experimental uncertainty due to photographic conditions.

respectively

$$\partial_t(h^2) + (h^2 v)' = 0 \tag{1}$$

$$\partial_t(\sigma h) + \left(\sigma h v + \frac{K^*}{2} h^2 E\right)' = 0 \tag{2}$$

$$\partial_t v + v v' = -\left(\frac{1}{h} - h'' - \frac{E^2}{8\pi} - 2\pi\sigma^2\right)' + \frac{2\sigma E}{\sqrt{\beta} h} + g^* + \frac{3\nu^{*2}}{h^2}(h^2 v')' \tag{3}$$

Here, $h(z)$ is the radius of the jet at axial coordinate z; $v(z)$ is the axial velocity of the jet and is constant across the jet cross-section to leading order; $\sigma(z)$ is the surface charge density, and $E(z)$ is the electric field in the axial direction. The prime ($'$) denotes differentiation with respect to z.

The non-dimensionalized tangential field inside the jet is derived from Coulomb's law

$$E = E_\infty + \int \mathrm{d}s \frac{\lambda(s)}{|x - r(s)|} \approx E_\infty + \ln\frac{r}{L}\left(\frac{\beta}{2}(h^2 E)' - \frac{4\pi}{\bar{\epsilon}} h\sigma\right) \tag{4}$$

where $\lambda(s)$ is the linear charge density along the jet, parametrized by the arclength s, and varying over a length scale L much larger than the jet radius.

4.2. Stable jets

The steady state jet profiles can be calculated numerically and compared to experiments. It should be noted that the one-dimensional model is an oversimplification of the real process immediately at the exit of the nozzle, and additional corrections were necessary in order to solve for stable jet profiles. First, the model assumes an infinitely long, slender jet. To ensure equipotential surfaces at a finite separation, d, as occurs in the experiments, a cascade of image charges was invoked for $z < 0$ and $z > d$. Stable solutions were then found for the low conductivity glycerol by assuming a boundary condition of $\sigma = 0$ at the top plate. This boundary condition is deemed plausible within the approximation of a one-dimensional model, since immediately at the exit of the nozzle, the charges have not had sufficient opportunity to relax from the bulk to the surface of the jet. Stable solutions for the higher conductivity PEO–water solutions, however, could not be found in the same way; we attribute this to inadequacies of the $\sigma = 0$ boundary condition. Second, achieving quantitative agreement between theory and experiment for glycerol required modification of the applied electric field experienced by the jet in the immediate vicinity of the nozzle to reflect the fringe field created by protrusion of the nozzle from the top plate that was used in the glycerol experiments. Local amplification of the applied electric field was calculated numerically using MATLAB©, based solely on the geometry of the protruding nozzle. With these semi-empirical modifications, quantitative agreement between theory and experiments could be obtained. The fringe field correction particularly emphasizes the importance of even small differences in equipment configuration between independent investigations, and the impact it can have on apparent operating behavior. Fig. 12 shows a comparison of experimental and theoretical jet profiles of glycerol; the agreement is encouraging.

4.3. Linear stability analysis

For the linear stability analysis, axisymmetric perturbations of the form $h^*/h = 1 + h_\epsilon \mathrm{e}^{\omega t + \mathrm{i}kz}$ were applied to the radius, where h_ϵ is assumed to be small. Similar perturbations in velocity, surface charge density and the local electric field strength were also introduced. A schematic representation of axisymmetric instabilities and the local variations in charge density are shown in Fig. 13(a). Substituting these perturbations into the governing hydrodynamic equations yields a dispersion relation for axisymmetric instabilities, which is shown in Eq. (5)

$$\omega^3 + \omega^2\left[\frac{4\pi K^* \Lambda}{\delta\sqrt{\beta}} + 3\nu^* k^2\right] + \omega\left[3\nu^* k^2 \frac{4\pi K^* \Lambda}{\delta\sqrt{\beta}} + \frac{k^2}{2}(k^2 - 1) + 2\pi\sigma_0^2 k^2\left(\frac{8\ell}{\delta} - 1\right) + \frac{\Lambda}{\delta}\frac{\Omega_0^2}{4\pi}k^2\right] + \frac{4\pi K^* \Lambda}{\delta\sqrt{\beta}}\left[\frac{k^2}{2}(k^2 - 1) + 2\pi\sigma_0^2 k^2 + \frac{\delta}{\Lambda}\frac{\Omega_0^2}{4\pi}k^2 + \frac{E_0\sigma_0}{\sqrt{\beta}}\mathrm{i}k\left(\frac{1}{\ell} - 4\right)\right] = 0 \tag{5}$$

where σ_0 is the (dimensionless) unperturbed charge density and $1/\chi$ is the local aspect ratio of the jet, indicative of the ratio of the jet diameter to the length scale over which the charge varies; its value is assumed to be small, in accord with the assumption of long wavelength instabilities. $\mathcal{L} = \ln(1/\chi)$, $\Lambda = \beta \ln(1/\chi)k^2$, and $\delta = 2 + \Lambda$.

The axisymmetric dispersion relation works for arbitrary values of conductivity, dielectric constant, viscosity and field strength, as long as the condition that the tangential electrical stress be smaller than the radial viscous stress is satisfied. It therefore permits comparison to experimental results. By taking special limits of Eq. (5), e.g. zero viscosity and infinite conductivity, excellent agreement with Saville's results [31], has been obtained [21,22].

Non-axisymmetric disturbances were modeled by considering long wavelength modulations of the jet centerline. The equations of motion are more complicated than Eqs. (1)–(3), due to allowance for bending. However, they are structurally similar to the equations for a slender elastic rod under slight bending [32]. When the jet bends, the charge density along the jet is no longer uniform around the circumference of the jet, but now also contains a dipolar component, $P(z)$, oriented perpendicular to the jet axis, as the internal charges adjust to screen the external field. These dipoles set up a localized torque that bends the jet, and oscillations of the bending instability account for the whipping motion of the jet. This is illustrated in Fig. 13(b). To derive the dispersion relation for non-axisymmetric disturbances, the centerline of the jet is described in non-dimensional coordinates by $\underline{r}(z,t) = z\hat{z} + \epsilon\, e^{\omega t + ikz}\hat{x}$, where $\hat{x}$ and $\hat{z}$ are unit vectors in a Cartesian coordinate system. The final form of the dispersion relation for non-axisymmetric disturbances is shown in Eq. (6)

$$\omega^2 + \frac{3}{4}\nu^*\omega k^4 + 4\pi\sigma_0^2 k^2 \ln(k) + ik\frac{2\sigma_0\Omega_0}{\sqrt{\beta}} + \frac{ik\Omega_0}{\sqrt{\beta}}(\sigma_0 k^2 + C) + k^2 - \left[\Omega_0\left(-\frac{1}{4\pi} + \frac{(\beta+1)k^2}{16\pi\beta}\right) + \frac{ik\sigma_0}{\beta}\right] \times \frac{\sqrt{\beta}}{\beta+2}[k^2\sqrt{\beta}\Omega_0 + ik(4\pi C + 2\pi\beta\sigma_0 k^2)] = 0 \quad (6)$$

with

$$C = -\frac{ik\frac{2K^*E_0}{\beta+2} + \frac{4\pi\sqrt{\beta}K^*}{\beta+2}\sigma_0 k^2}{\frac{4\pi\sqrt{\beta}K^*}{\beta+2} + \omega}$$

The non-axisymmetric dispersion relation has also been compared to special cases, e.g. inviscid jets without surface charge or perfect conductors [31], and the agreement is again excellent.[1]

Evaluating the dispersion relations, three different types of instabilities are predicted: two axisymmetric modes and one non-axisymmetric mode. The first axisymmetric mode can be associated with the classical Rayleigh instability, which is dominated by surface tension. The Rayleigh instability is suppressed at high electric fields and therefore irrelevant for electrospinning. In addition, however, there are two electrically driven modes, which we refer to as 'conducting' modes because at high electric field they are primarily sensitive to the fluid conductivity and insensitive to surface tension. The first of these modes is axisymmetric, while the second is non-axisymmetric ('whipping'). It is the competition between the two conducting modes that is of importance at the high-applied fields typical of the electrospinning process. The mode that dominates depends critically on both the surface charge density and the radius of the jet as the jet thins away from the nozzle. These quantities must either be obtained from calculations of the jet profile or measured independently.

Finally, drawing on the empirical observation that the instabilities grow as they are convected downstream, and assuming that the growth rate for each mode may be characterized by the maximum in the corresponding dispersion curve, that each mode is independent of all other modes, and that the instantaneous growth rates are functions only of the local conditions along the otherwise stable jet, one can compute the relative growth rates of competing instability modes. Let $A(t)$ denote the amplitude of a perturbation to the jet at time t. Then

$$\frac{1}{A}\frac{dA}{dt} = \omega(h, E, \sigma) \quad (7)$$

where ω is the calculated growth rate of the perturbation subject to the instantaneous local conditions of jet radius, charge density and local electric field. Such a perturbation is convected downstream with a velocity $U = Q/(\pi h^2)$. Making the approximation that $dA/dt \approx U(dA/dz)$, where z measures the distance along the jet, yields a formula for the amplification factor Γ of the perturbation after it convects a

[1] Direct comparison to a recently reported mathematical description of the jet by Reneker et al. [30] is complicated by their choice of a mechanistic model that attributes charge to a set of imaginary beads whose geometric disposition is prescribed by deformation of discrete, viscoelastic elements. By its construction, the model of Ref. [30] imposes assumptions that the charge distribution is axisymmetric to the local jet axis, that charge transport is entirely convective and that jet instability can occur only through bending. It is thus not predictive for regimes of operation or mechanism of instability. In addition, several quantities of that model are difficult to measure accurately (e.g. the perturbation frequency ω) or do not apply to Newtonian fluids (e.g. elastic modulus, G), where bending is also observed (see, for example, Ref. [33]). Even assuming reasonable values for most parameters, for example, Ref. [30] reports modeling at an electric field (V/h) which is an order of magnitude smaller than the experimental value, in order to obtain qualitative agreement. This discrepancy has recently been modified by introducing into the model a variable viscosity, attributable to changing polymer concentration as solvent evaporates Ref. [34].

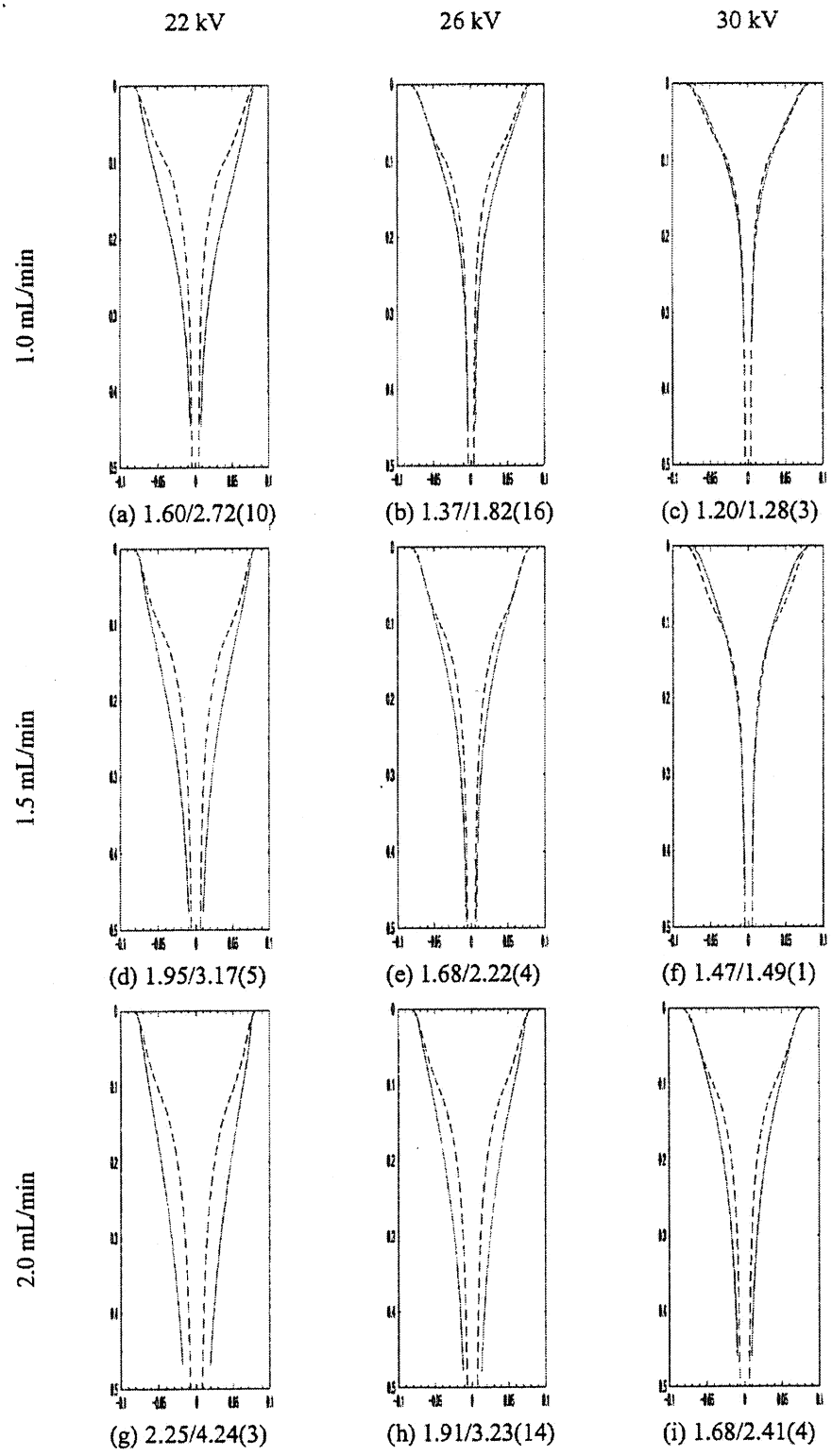

Fig. 12. Comparison of theoretical (dashed) and experimental (solid) profiles for a glycerol jet. The plate distance is 6 cm and the nozzle protrusion is 7.2 mm. The agreement is best for low flow rates and high fields (b, c, e, f). The pair of numbers beneath each plot is the theoretical healing length/experimental healing length, normalized to the outer diameter of the nozzle. The healing length is defined as the distance over which the initial radius of the jet decreases by a factor of $1/e$.

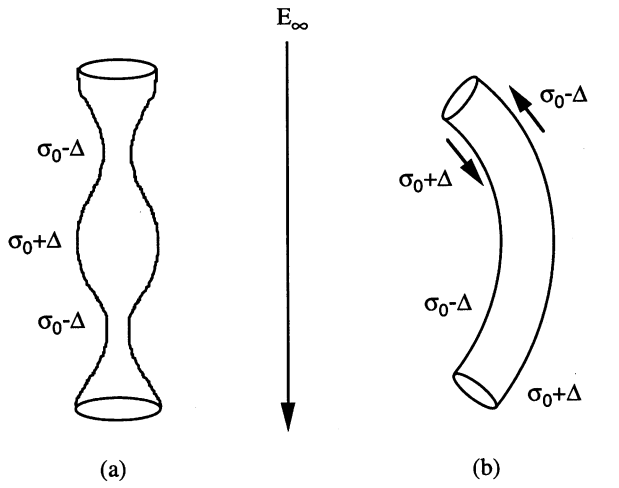

Fig. 13. (a) Axisymmetric and (b) non-axisymmetric instabilities in a fluid jet in an external electric field (E_∞). Δ denotes perturbations of the surface charge density (σ). The arrows in (b) indicate the local torque that bends the jet.

distance, d, downstream

$$\Gamma(E_\infty, Q) = \log\left[\frac{A(d)}{A(0)}\right] = \int_0^d \frac{\omega(h, E, \sigma)\pi h^2}{Q} \tag{8}$$

Theoretical operating diagrams were calculated using Eq. (8). These are in essence contour maps of $\Gamma(E_\infty,Q)$. Fig. 5 shows a comparison of theoretical and experimental operating diagrams for glycerol. The boundaries between operating regimes were computed by assuming that the instability grows by a factor of $e^{2\pi}$ by the time it has convected from the top plate to the bottom plate. The agreement between theory and experiments is encouraging, given the number of simplifying approximations invoked to construct the theoretical diagrams. In Fig. 9, the corresponding comparison for the PEO–water solution is shown, assuming the same amplification. Again, the agreement between theory and experiments is good. It should be noted that the experimentally observed concavity of the transition from stable jets to unsteady jets is also captured by the theory.

5. Conclusions

A systematic experimental and theoretical analysis suggests that a suitable description of the electrospinning process may be captured through the use of operating diagrams of electric field versus flow rate. A third operating parameter, the electric current, is also crucial but not an independent parameter in the experimental realization of the process. The current is a measure of the charge density carried by the jet and depends on the manner in which charge is induced in the fluid. Thus, it appears to depend not only on fluid parameters such as conductivity, but also on equipment configuration, such as the geometry of the high voltage electrode, through its impact on the shape of the local electric field in the vicinity of the spinneret. A key step in the formation of submicron diameter solid fibers by electrospinning appears to involve a fluid instability, the rapidly whipping jet. The experimental observations are supported by a newly developed theory for electrified fluid jets. The good agreement between experiments and theory indicates that the mechanism involves a whipping jet, which is caused by the interaction between the external electric field and the surface charges of the jet. Based on these observations, it is conjectured that the large diameter reduction in electrospinning is achieved by stretching and acceleration of a fluid filament in the instability region prior to solidification or impact on the collector.

Acknowledgements

The authors are grateful to G. McKinley, L.P. Kadanoff, L. Mahadevan, D. Saville, I. Cohen, S. Warner and D. Reneker for valuable discussions. MMH acknowledges support from the MRSEC at the University of Chicago, as well as support from an NSF grant to L.P. Kadanoff. MMH and MPB gratefully acknowledge support from the Donors of the Petroleum Research Fund, administered by the American Chemical Society, for partial support of this research, and the NSF Division of Mathematical Sciences. Financial support for the experimental work was provided by grants from the National Science Foundation (CTS-945711) and the National Textile Center (M98-D01) to GCR.

References

[1] Ziabicki A. Fundamentals of fibre formation: the science of fiber spinning and drawing. New York: Wiley, 1976.
[2] How TV. US Patent 4,552,707, 1985.
[3] Simm W, Gösling C, Bonart R, von Falkai B. US Patent 4,069,026, 1978.
[4] Gibson PW, Schreuder-Gibson HL, Rivin D. AIChE J 1999;45:190–5.
[5] Formhals A. US Patent 1,975,504, 1934.
[6] Larrondo L, St. John Manley R. J Polym Sci, Polym Phys Ed 1981;19:909–20.
[7] Larrondo L, St. John Manley R. J Polym Sci, Polym Phys Ed 1981;19:921–32.
[8] Larrondo L, St. John Manley R. J Polym Sci, Polym Phys Ed 1981;19:933–40.
[9] Doshi J, Reneker DH. J Electrostatics 1995;35:151–60.
[10] Srinivasan G, Reneker DH. Polym Int 1995;36:195–201.
[11] Reneker DH, Chun I. Nanotechnology 1996;7:216–23.
[12] Fong H, Chun I, Reneker DH. Polymer 1999;40:4585–92.
[13] Gibson P, Schreuder-Gibson H, Pentheny C. J Coated Fabrics 1998;28:63–72.
[14] Taylor GI. Proc Roy Soc Lond (A) 1964;280:383–97.
[15] Cloupeau M, Prunet-Foch B. J Electrostatics 1989;22:135–59.
[16] Baumgarten PK. J Colloid Interface Sci 1971;36(1):71–9.
[17] Doshi J. PhD Thesis, University of Akron, 1994.
[18] Jaeger R, Bergshoef MM, Martin-i-Batlle C, Schoenherr H, Vansco GJ. Macromol Symp 1998;127:141–50.

[19] Deitzel JM, Kleinmeyer J, Harris D, Beck Tan NC. Polymer 2001;42:261–72.
[20] Shin YM, Hohman MM, Brenner MP, Rutledge GC. Appl Phys Lett 2001;78(8):1149–51.
[21] Hohman MM, Shin YM, Brenner MP, Rutledge GC. Phys Fluids 2001;13:2201.
[22] Hohman MM, Shin YM, Brenner MP, Rutledge GC. Phys Fluids 2001;13:2221.
[23] Lide D, editor. CRC handbook of chemistry and physics, 79th ed. Cleveland: CRC Press, 1998.
[24] Hayati I. Colloids and surfaces 1992;65:77–84.
[25] Melcher JR, Taylor GI. Annu Rev Fluid Mech 1969;1:111–46.
[26] Kirichenko VN, Petryanov-Sokolov IV, Suprun NN, Shutov AA. Sov Phys Dokl 1986;31(8):611–3.
[27] Taylor GI. Proc Roy Soc Lond A 1969;313:453–75.
[28] Fong H, Reneker DH. Electrospinning and the formation of nanofibers. In: Salem DR, editor. Structure formation in polymeric fibers. Munich: Hanser, 2001. p. 225–46.
[29] Warner SB, Buer A, Ugbolue SC, Rutledge GC, Shin YM. National Textile Center Annual Report, 1998, M98-D01: 83-90.
[30] Reneker DH, Yarin AL, Fong H, Koombhongse S. J Appl Phys 2000;87(9):4531–47.
[31] Saville DA. J Fluid Mech 1971;48(4):815–27.
[32] Landau LD, Lifshitz EM. Theory of elasticity. Reading: Addison Wesley, 1959.
[33] Taylor G. Proc Roy Soc Lond A 1969;313:453.
[34] Yarin AL, Koombhongse S, Reneker DH. J Appl Phys 2001;89:3018.